

Weak Gravitational Lensing and its Cosmological Applications

HENK HOEKSTRA

*Department of Physics and Astronomy, University of Victoria, 3800 Finnerty
Road, Victoria, BC, V8P 5C2, Canada. Email:hoekstra@uvic.ca*

BHUVNESH JAIN

*Department of Physics and Astronomy, University of Pennsylvania,
Philadelphia, PA 19104. Email: bjain@physics.upenn.edu*

Key Words gravitational lensing,dark matter,dark energy,cosmology

Abstract

Weak gravitational lensing is a unique probe of the dark side of the universe: it provides a direct way to map the distribution of dark matter around galaxies, clusters of galaxies and on cosmological scales. Furthermore, the measurement of lensing induced distortions of the shapes of distant galaxies is a powerful probe of dark energy. In this review we describe how lensing measurements are made and interpreted. We discuss various systematic effects that can hamper progress and how they may be overcome. We review some of the recent results in weak lensing by galaxies, galaxy clusters and cosmic shear and discuss the prospects for dark energy measurements from planned surveys.

CONTENTS

Introduction	2
How to measure shear	4
<i>Weak lensing basics</i>	4
<i>Weak lensing pipeline</i>	5
<i>Diagnostics of the lensing signal</i>	7
<i>Tests on simulated images</i>	8
Cosmic shear and dark energy	9
<i>Two-point shear correlations and tomography</i>	9
<i>Cross-correlations and higher order statistics</i>	10
<i>Cosmological parameters</i>	12
Systematic errors	14
<i>Intrinsic alignments</i>	14
<i>How systematics degrade cosmological constraints</i>	15
Observational results	17
<i>Implications for cosmology</i>	19
Lensing by galaxies and galaxy clusters	20
<i>Mapping the distribution of dark matter</i>	20
<i>Cosmology with galaxy clusters</i>	21
<i>Properties of dark matter halos</i>	23
The Future	24
<i>Planned surveys</i>	25
<i>Prospects for lensing cosmology</i>	27

1 Introduction

The deflection of light rays by intervening structures, a phenomenon referred to as gravitational lensing, provides astronomers with a unique tool to study the distribution of dark matter in the universe. Unlike other observational probes, the lensing effect provides a direct measure of the mass, irrespective of the dynamical state of the lens. A well publicized recent example is the study of the merging ‘Bullet’ cluster of galaxies, in which a lensing study showed that the dark matter

is displaced from the bulk of the baryonic mass (1). Such measurements can provide important insights into the properties of dark matter.

A number of applications of gravitational lensing have proven important for observational cosmology. When the lens is sufficiently strong, multiple images of the same source can be observed. If the source is variable, time delays between the variation of the images can be determined. An example of the applications of strong lensing is in the use of time delays to estimate the Hubble constant, provided a good model for the lens can be derived (see e.g. (2,3)). In this review, however, the focus will be on applications of weak gravitational lensing that can help us understand the properties of dark energy and dark matter on cosmological scales.

Weak lensing refers to the shearing of distant galaxy images due to the differential deflection of neighboring light rays. The signal is small, typically inducing an ellipticity of order 1%. While this is negligible compared to the intrinsic shape of individual galaxies, it can be measured statistically using the coherence of the lensing shear over the sky. In the past two decades it has become possible to measure these subtle changes to study the distribution of dark matter in the universe. The first measurements used lensing by galaxy clusters; more recently cosmic shear measurements have been made in “blank fields”, without using any knowledge of foreground structures. A number of topics related to galaxy and cluster lensing are discussed in §5, but the main focus of this review is cosmic shear, i.e. lensing by large-scale structure in the universe.

The reason for the recent popularity of cosmic shear is the fact that the signal is a direct measure of the projected matter power spectrum over a redshift range determined by the lensed sources (see e.g., (4,5)). This straightforward interpretation of the signal is rather unique in the tools available for cosmology, and it potentially enables the determination of cosmological parameters with high precision. Lensing measurements are not only sensitive to the geometry (similar to distance measures such as type Ia supernovae or baryonic acoustic oscillations), but also provide measures of the growth of large-scale structure that test gravity on cosmological scales. These features make cosmic shear one of the most powerful probes of dark energy and modified gravity theories (6,7), albeit an observationally challenging one.

This review focuses on the methods and principal challenges in the cosmological applications of weak lensing. We review lensing theory but the focus is on measurements, current surveys and prospects for planned surveys in the coming decade. We refer the interested reader to reviews with a more detailed treatment of many other aspects of lensing (8,9,10,11).

In §2, we describe the key steps in the measurement and in §3 we discuss the interpretation of cosmological weak lensing. In §4 we review the primary systematic errors, as well as ways to deal with them. We highlight some of the current results in cosmological weak lensing in §5. In §6 we discuss lensing by galaxies and galaxy clusters. We conclude in §7 with a discussion of prospects

for the coming decade.

2 How to measure shear

2.1 Weak lensing basics

Massive structures along the line of sight deflect photons originating from distant galaxies. If the source is small, the effect is a (re)mapping of f^s , the source's surface brightness distribution (see Reference (8) for more details):

$$f^{\text{obs}}(\theta_i) = f^s(\mathcal{A}_{ij}\theta_j), \quad (1)$$

where \mathcal{A} is the distortion matrix (the Jacobian of the transformation)

$$\mathcal{A} = \frac{\partial(\delta\theta_i)}{\partial\theta_j} = (\delta_{ij} - \Psi_{,ij}) = \begin{pmatrix} 1 - \kappa - \gamma_1 & -\gamma_2 \\ -\gamma_2 & 1 - \kappa + \gamma_1 \end{pmatrix} \quad (2)$$

where we have introduced the two-dimensional lensing potential Ψ , and where $\Psi_{,ij} \equiv \partial^2\Psi/\partial\theta_i\partial\theta_j$. The lensing convergence κ is a scalar quantity and is given by a weighted projection of the mass density fluctuation field:

$$\kappa(\boldsymbol{\theta}) = \frac{1}{2}\nabla^2\Psi(\boldsymbol{\theta}) = \int d\chi W(\chi)\delta[\chi, \chi\boldsymbol{\theta}], \quad (3)$$

with the Laplacian operator ∇^2 defined using the flat sky approximation as $\nabla^2 \equiv \partial^2/\partial\boldsymbol{\theta}^2$ and χ is the comoving distance (we have assumed a spatially flat universe). Note that χ is related to redshift z via the relation $d\chi = dz/H(z)$, where $H(z)$ is the Hubble parameter at epoch z . The lensing efficiency function W is given by

$$W(\chi) = \frac{3}{2}\Omega_{m0}H_0^2a^{-1}(\chi)\chi \int d\chi_s n_s(\chi_s)\frac{\chi_s - \chi}{\chi_s}, \quad (4)$$

where $n_s(\chi_s)$ is the redshift selection function of source galaxies and H_0 is the Hubble constant today ($H_0 = 100h \text{ km s}^{-1}\text{Mpc}^{-1}$). If all source galaxies are at a single redshift z_s , then $n_s(\chi) = \delta_D(\chi - \chi_s)$.

In Equation 2 we introduced the components of the complex shear $\boldsymbol{\gamma} \equiv \gamma_1 + i\gamma_2$, which can also be written as $\boldsymbol{\gamma} = \gamma \exp(2i\alpha)$, where α is the orientation angle of the shear. The Cartesian components of the shear field are related to the lensing potential through

$$\gamma_1 = \frac{1}{2}(\Psi_{,11} - \Psi_{,22}) \quad \text{and} \quad \gamma_2 = \Psi_{,12}, \quad (5)$$

In the weak lensing regime, the convergence gives the magnification (increase in size) of an image and the shear gives the ellipticity induced on an initially circular image. Under the assumption that galaxies are randomly oriented in the absence of lensing, the strength of the tidal gravitational field can be inferred from the measured ellipticities of an ensemble of sources (see §4.2 for a discussion

of intrinsic alignments). In the absence of observational distortions, the observed ellipticity e^{obs} is related to its unlensed value e^{int} through (12, 8):

$$e^{\text{obs}} = \frac{e^{\text{int}} + \gamma}{1 + \gamma^* e^{\text{int}}}, \quad (6)$$

where $e \simeq [(1 - b/a)/(1 + b/a)] \exp(2i\alpha)$ for an ellipse with major and minor axes a and b , respectively, and orientation angle α . γ^* is the complex conjugate of the lensing shear. The average value of $e^{\text{obs}} \approx \gamma$ in the weak lensing regime. To be more precise, the observable is the reduced shear $\gamma/(1 - \kappa)$. Hence, the unbiased measurement of the shapes of background galaxies (which constitute the small, faint end of the galaxy sample) lies at the heart of any weak lensing analysis.

2.2 Weak lensing pipeline

The unbiased measurement of galaxy shapes is not a trivial task, because the observed images have been ‘corrupted’: even in space based data, the finite size of the mirror and the complicated telescope optics give rise to a non-trivial point spread function (PSF). In ground based data the situation is worse because of turbulence in the atmosphere (an effect called seeing). Finally, the image is sampled in discrete pixels (which may not be square), with a detector that may suffer from charge transfer inefficiencies or other detector non-linearities.

The combination of seeing and the intrinsic size of the PSF leads to a circularization of the observed images, whereas PSF anisotropy introduces coherent alignments in the shapes of the galaxies. The former effect lowers the amplitude of the inferred lensing signal; the latter can mimic a lensing signal. Hence, to infer the true lensing signal, one needs to determine the original galaxy shape: this requires some form of deconvolution in the presence of noise. It is therefore not surprising that the development of methods that can undo the effects of the PSF has been a major focus of lensing research.

We list below the schematic steps of a pipeline that starts with raw galaxy images and that ultimately delivers cosmological measurements (see (13) for details and discussion of potential systematic errors at each step).

1. Object detection: The detection of the faint galaxies that are used in the analysis forms the first step in the lensing analysis. This can be done on the individual exposures (as multiple images of the same area of sky are typically obtained) or on a stacked image. In either case, an algorithm to distinguish stars from galaxies is needed. Note also that the images need to be corrected for any shearing by the camera. The next step is to quantify shape parameters for these objects. The optimal way to detect galaxies and measure their shapes using multiple exposures and a set of filters is an area of ongoing research which we will not address further.

2. PSF estimation: To deal with the effects of the point spread function (PSF) a sample of moderately bright stars is identified from the actual data.

These are subsequently used to characterise the PSF in terms of its size, second moment and possibly higher moments.

The variation of the PSF across the field of view is described with an interpolating function, which is typically done using a simple polynomial model (14). This appears to be adequate for current results, but ultimately the accuracy is limited by the fact that only a limited number of stars is observed. One way to address this issue is to study the PSF in observations with a high number density of stars (14). However, it is reasonable to assume that the PSF varies in a relatively systematic fashion from exposure to exposure. This allows one to decompose the observed patterns into their principal components, as proposed by (15). As the accuracy of cosmic shear measurements improves, such a careful modeling of the PSF will likely be required in order to undo the effects of the PSF.

3. PSF correction: Having identified the galaxies of interest, the next step is to correct the observed galaxy shapes for the convolution by the PSF. This is arguably the most difficult, yet most important step in the analysis. This is one of the most active areas of study and innovation, not only to derive reliable results from the current generation of surveys, but also to ensure that future, much more demanding, cosmic shear surveys can reach their full potential.

A number of techniques have been developed to address this problem and (16, 17) provide detailed descriptions of these. The most widely used method, the KSB method, was developed by (18). This is also one of the oldest methods, although modifications were suggested by (19, 20). The KSB method assumes that the PSF can be described as the convolution of a compact anisotropic kernel and a large isotropic kernel. Although this may appear to be a reasonable assumption for ground based data, it is not correct for space based data (20). A nice feature of the method is that the correction for PSF anisotropy and the circularization by the PSF are separate operations. The latter step (the closest to the actual deconvolution) is typically performed by averaging the correction for objects of similar size.

The KSB approach is limited by the assumptions that have to be made about the PSF and galaxy profiles. Relaxing such assumptions and expanding the object surface brightness distribution using a suitable set of basis functions has attracted much attention in recent years (21, 22, 23, 24). A related approach is to fit versatile models to the data and perform the deconvolution using the best fit models. For instance (25) explored whether objects can be modeled as sums of Gaussians. An advantage of the model fitting methods is that pixelation effects are readily implemented. Although progress is being made, it is currently unclear what the best procedure will be.

4. Measurement of shear correlations and cosmological parameters: Once a catalog of galaxy shapes is available, cosmological statistics can be calculated. The two-point correlations of the shear are calculated simply from the galaxy positions, ellipticities, and weights that characterize the signal-to-noise

of the shape measurement. These may be calculated as a power spectrum or correlation function for varying angular separations. For other applications to galaxy and cluster lensing, one works with the background shapes with reference to foreground objects.

Cosmological inferences rely on one additional property of the source galaxies, namely their redshift. The galaxies of interest are too faint to be observed spectroscopically. Instead, weak lensing studies rely on photometric redshifts (henceforth photo- z 's). These are based on the measured galaxy colors and other properties that provide a coarse estimate of the galaxy's redshift. Improvements in photo- z estimation and quantifying the effect of photo- z errors on cosmological inferences from lensing are both active areas of research.

2.3 Diagnostics of the lensing signal

An obvious concern is that one cannot “see” the weak lensing signal: a weakly sheared galaxy appears unchanged, because of its much larger intrinsic ellipticity. How can we be sure that the recovered lensing signal is cosmological in nature, and not dominated by observational distortions?

As discussed below, we can test the weak lensing analysis pipeline on simulated data, but these simulations may lack a systematic effect that is present in real data. Fortunately, a number of diagnostic tools can be used to test the reliability of the recovered lensing signal. These tests cannot guarantee whether the recovered signal is free of systematics, but they do often indicate whether systematics are present. (Note, however, that the correction for the circularization by the PSF cannot be tested using the diagnostics discussed below.)

The first diagnostic makes use of the fact that the corrected galaxy shapes should not correlate with the (uncorrected) shapes of stars (e.g., (26)). The measurement of this correlation is sensitive to imperfections in the model for PSF anisotropy and imperfections in the correction scheme itself. The former can be tested by correlating the corrected shapes of stars (14).

Another unique diagnostic makes use of the fact that the weak lensing shear arises from a gravitational potential. Consequently, the resulting shear field is expected to be curl-free (see, however, (27)). The observed ellipticity correlation functions can be separated into two independent components, an “E”-mode which is curl-free and a “B”-mode, which is sensitive to the curl of the shear field (28,27). Hence, the presence of a significant “B”-mode indicates that residual systematics remain. (Note that the “B”-mode may also have a physical origin, caused by intrinsic alignments of the sources – see §4.2 for more details.)

A diagnostic of the cosmological nature of the lensing signal is its variation with redshift. The distance factors in the lensing efficiency function of Equation 4 lead to a characteristic variation with source redshift. Thus, provided the redshift estimates are accurate, this variation can be used to test the cosmological origin of the lensing signal. Another diagnostic that we discuss below is the use of

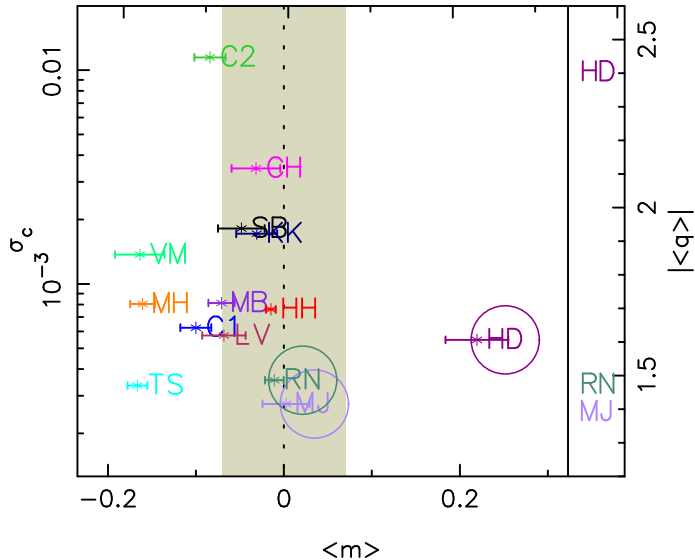


Figure 1: Measurement of the the calibration bias m and PSF residuals σ_c from (16). The ideal method has $m = 0$ and small σ_c . The shaded region indicates a bias of less than 7%. Methods that were used for the most recent published cosmic shear results were found to have biases of the order of a few percent. We refer the reader to (16) for a detailed description of the symbols and methodology.

different statistical measures, such as two- and three-point shear correlations, that have a distinct relationship for a signal due to gravitational lensing. Finally, one can compare different lensing observables, such as those related to shear and to magnification effects.

2.4 Tests on simulated images

The main hurdle in the shape measurement is a proper handling of the PSF-induced systematics, not our lack of understanding of the relevant physics. Our ability to correct for shape measurement systematics can therefore be tested using simulated data, which is an important advantage of lensing over other methods.

The Shear TESting Programme (STEP) is a collaborative effort involving much of the weak lensing community to improve the accuracy of weak lensing measurements, in preparation for the next generation of cosmic shear surveys. The first STEP paper (16) involved the blind analysis of simulated ground based images. The galaxies in this simulation had relatively simple morphologies; however, despite these limitations, the results provided an important benchmark for the accuracy of current ground-based weak lensing analysis methods.

The results of this exercise are shown in Figure 1. The dominant source of error is the correction for the size of the PSF, which leads to an overestimate of the shear by a multiplicative factor $(1 + m)$. A blind analysis of more com-

plicated galaxies was presented in (17), which also included an improvement in the statistical accuracy of the test. These two studies showed that pipelines that have been used to constrain cosmological parameters can recover the lensing signal with a precision better than 7%, within the statistical errors of current weak lensing analyses. The most successful methods were shown to achieve 1-2% level accuracy. Although sufficient for current work, biases as a function of object size and magnitude remain. The next phase in this work is to identify the points of failure and find improvements. The simulations also need to become more realistic, for instance through the inclusion of systematics at the detector level.

3 Cosmic shear and dark energy

3.1 Two-point shear correlations and tomography

To quantify the lensing signal, we measure the shear correlation functions from galaxy shape catalogs. The two-point correlation function of the shear, for source galaxies in the i -th and j -th redshift bin, is defined as

$$\xi_{\gamma_i \gamma_j}(\theta) = \langle \gamma_i(\boldsymbol{\theta}_1) \cdot \gamma_j^*(\boldsymbol{\theta}_2) \rangle. \quad (7)$$

with $\theta = |\boldsymbol{\theta}_1 - \boldsymbol{\theta}_2|$. Note that the two-point function of the convergence is identical to that of the shear. It is useful to separate ξ_γ into two separate correlation functions by using the $+/\times$ decomposition: the $+$ component is defined parallel or perpendicular to the line connecting the two points taken, while the \times component is defined along 45° . This allows us to define the rotationally invariant two-point correlations of the shear field: $\xi_+(\theta) = \langle \gamma_{i+}(\boldsymbol{\theta}_1) \gamma_{j+}(\boldsymbol{\theta}_2) \rangle$, and $\xi_\times(\theta) = \langle \gamma_{i\times}(\boldsymbol{\theta}_1) \gamma_{j\times}(\boldsymbol{\theta}_2) \rangle$. The correlation function of Equation 7 is simply given by $\xi_{\gamma_i \gamma_j} = \xi_+ + \xi_-$.

The E/B mode decomposition discussed in §2.3 is given by linear superpositions of $\xi_+(\theta)$ and $\xi_\times(\theta)$ (though it involves integrals over all θ). A more direct way to perform the E/B decomposition is through the mass aperture variance, $M_{\text{ap}}^2(\theta)$, which is a weighted second moment of the tangential shear measured in apertures. This provides a very useful test of systematics in the measurements; we will not use it here, but refer the reader to (27). All two-point statistics such as $M_{\text{ap}}^2(\theta)$ can be expressed in terms of the shear correlation functions defined above.

The shear power spectrum at angular wavenumber ℓ is the Fourier transform of $\xi_{\gamma_i \gamma_j}(\theta)$. It is identical to the power spectrum of the convergence and can be expressed as a projection of the mass density power spectrum P_δ . For source galaxies in the i th and j th redshift bin it is (5, 29)

$$C_{\gamma_i \gamma_j}(\ell) = \int_0^\infty dz \frac{W_i(z) W_j(z)}{\chi(z)^2 H(z)} P_\delta\left(\frac{\ell}{\chi(z)}, z\right). \quad (8)$$

where the indices i and j cover all the redshift bins. The redshift binning is assumed to be provided by photo- z 's that can be estimated from multi-color

imaging. If both source galaxy bins are taken at redshift z_s , then the integral is dominated by the mass fluctuations at a distance about half-way to the source galaxies. Figure 2 shows the predicted auto and cross-spectra for galaxies split into two redshift bins. The error bars show the sample variance (which dominates at low ℓ) and intrinsic ellipticity (which dominates at high ℓ) contribution to the measurement error. The latter is also referred to as shape noise in the literature. (Note that the measured power spectrum includes contributions from systematic errors, which we discuss in §4.)

Equation 8 shows how the observable shear-shear power spectra are sensitive both to the geometric factors given by $W_i(z)$ and $W_j(z)$, as well as to the growth of structure contained in the mass density power spectrum P_δ . Both are sensitive to dark energy and its possible evolution which determines the relative amplitudes of the auto and cross-spectra shown in Figure 2. P_δ also contains information about the primordial power spectrum and other parameters such as neutrino masses. In modified gravity theories, the shape and time evolution of the density power spectrum can differ from that of a dark energy model, even one that has the same expansion history. Lensing is a powerful means of testing for modifications of gravity as well (30,31,32,33,34). The complementarity with other probes of each application of lensing is critical, especially with the CMB and with measurements of the distance-redshift relation using Type Ia Supernovae and baryonic acoustic oscillations in the galaxy power spectrum.

The mass power spectrum is simply related to the linear growth factor $D(z)$ on large scales (low ℓ): $P_\delta \propto D^2(z)$. However, for source galaxies at redshifts of about 1, observable scales $\ell \gtrsim 200$ receive significant contributions from non-linear gravitational clustering. So we must go beyond the linear regime using simulations or analytical fitting formulae to describe the nonlinear mass power spectrum (35,36,37,38). To the extent that only gravity describes structures on scales larger than the sizes of galaxy clusters, this can be done with high accuracy. There is ongoing work to determine what this scale precisely is and how to model the effect of baryonic gas on smaller scales (39).

3.2 Cross-correlations and higher order statistics

The cross-correlation of foreground galaxy positions with background shear is also an observable. As discussed in §6, it has been measured by averaging the tangential component of the background galaxy ellipticities in circular annuli centered on the foreground galaxy. It is denoted $\langle \gamma_T \rangle(\theta)$ and is related to the Fourier transform of the galaxy-convergence power spectrum, which in turn can be expressed analogously to the power spectrum of equation 8:

$$C_{g_i \kappa_j}(\ell) = \int_0^\infty dz \frac{W_{g_i}(z) W_j(z)}{\chi(z) H(z)} P_{g\delta} \left(\frac{\ell}{\chi(z)}, z \right), \quad (9)$$

where W_{g_i} is the normalized redshift distribution of the lens (foreground) galaxies and $P_{g\delta}$ is the three-dimensional galaxy-mass density power spectrum.

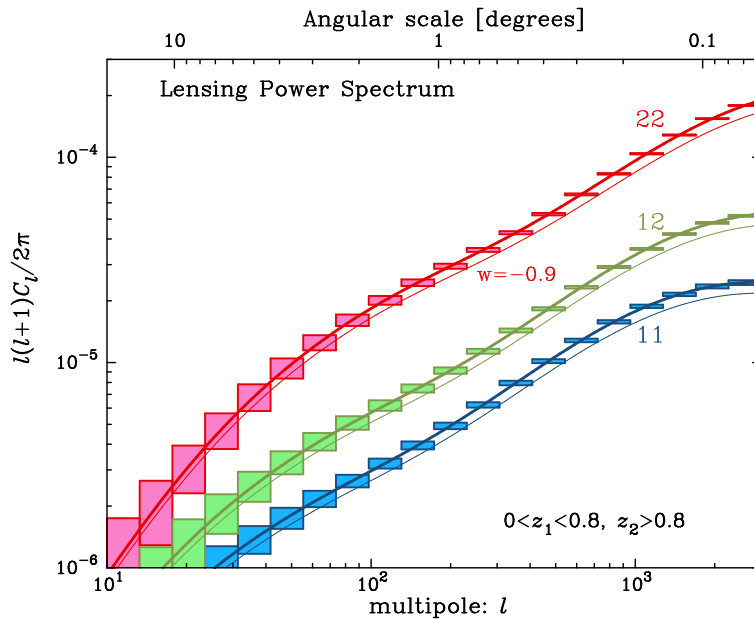


Figure 2: The lensing power spectra constructed from galaxies split into two broad redshift bins. The two auto-spectra and one cross-spectrum are shown. The solid curves are predictions for the fiducial Λ CDM model, which include nonlinear evolution (40). The boxes show the expected measurement error due to the sample variance and intrinsic ellipticity errors from a 5000 deg^2 survey with median redshift $z = 0.8$ (these are ambitious survey parameters by the standards of Stage III surveys). The thin curves are the predictions for a dark energy model with $w = -0.9$. Note that at least four or five redshift bins are expected to be useful from such a survey, leading to many more measured power spectra.

Along with the galaxy-galaxy power spectrum, $C_{g_i g_i}(\ell)$, equations 8 and 9 represent the three sets of auto- and cross-spectra that can be measured from (foreground) galaxy positions and (background) galaxy shapes (41). Each of the three power spectra can be measured for multiple photo- z bins. These contain all the two-point information one can extract from multicolor imaging data on both galaxy clustering and lensing. It would be an exhaustive exercise in parameter estimation to perform model fitting on a set of such measurements; only pieces of this have been carried out so far.

In addition, cosmographic information via the distance-redshift relation can be obtained using the variation of the galaxy-galaxy lensing signal with redshift. While this has less constraining power than other tests of the distance-redshift relation, it would help isolate the geometric and growth of structure information

that can be obtained from lensing (42, 41, 43, 44, 45).

The combination of $C_{g_i g_i}(\ell)$ and $C_{g_i \kappa_j}(\ell)$ can be used to determine the bias factor b that relates the three-dimensional galaxy power spectrum to that of the mass density (the ratio of the two for appropriate redshift bins is proportional to b). With this empirical determination of b , cosmological parameters can be obtained more robustly from $C_{g_i g_i}(\ell)$ and its three-dimensional counterpart measured from spectroscopic surveys (46). Planned surveys with good quality imaging and well calibrated photo-z's will enable cosmological applications of $C_{g_i \kappa_j}(\ell)$ as well, once the bias is known for the lens galaxies as a function of scale.

Thus a variety of cosmological measurements can be made from lensing and galaxy power spectra. The two main advances awaiting these applications are reliable photo-z's and lensing shapes measured over a wide area survey.

Finally, the non-Gaussian properties of the lensing mass imprints three-point and higher order correlations in the shear field. These are valuable both for complementary cosmological information and for checks on systematic errors (47, 48). The lensing three-point function, or bispectrum in Fourier space, arises from non-linear gravitational evolution of the lensing mass. It vanishes at lower order in perturbation theory, as the leading order (linear) density field is Gaussian random. The second order contributions to the bispectrum give it special value: its dependence on cosmological parameters differs from that of the power spectrum. In particular, it is possible to combine the power spectrum and bispectrum to constrain the matter or dark energy density with little dependence on the power spectrum amplitude (47, 35, 40).

The signal-to-noise ratio for a measurement of the bispectrum is lower than for the power spectrum, and is more sensitive to the number density of source galaxies. While three-point lensing correlations have been detected in current data, it is expected to be useful for cosmology only in next generation datasets. Perhaps of equal importance is the ability to test for systematic errors using three-point correlations. (48) showed how the degradation due to systematics can be reduced by adding bispectrum and power spectrum measurements.

3.3 Cosmological parameters

Given a data vector, the Fisher information matrix describes how errors propagate into the precision on cosmological parameters p_α . The Fisher matrix applied to the lensing power spectra is given by

$$F_{ij} = \sum_{\ell} \left(\frac{\partial \mathbf{C}}{\partial p_i} \right)^T \mathbf{Cov}^{-1} \frac{\partial \mathbf{C}}{\partial p_j}, \quad (10)$$

where \mathbf{C} is the column matrix of the observed power spectra and \mathbf{Cov}^{-1} is the inverse of the covariance matrix between the power spectra. The partial derivative with respect to a parameter p_α is evaluated around the fiducial model. The Fisher matrix quantifies the best statistical errors achievable on parameter

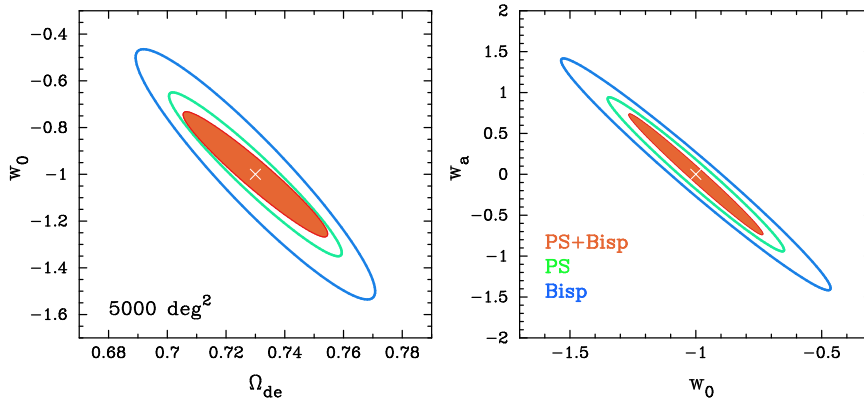


Figure 3: Dark energy contours (68.3% confidence level) from lensing power spectra and bispectra from an ambitious Stage III survey, as in Figure 2. The estimated non-Gaussian covariances between the power spectra and bispectra are included in the joint constraints. These forecasts assume Planck priors and do not include systematic errors.

determination with a given data set: the variance of an unbiased estimator of a parameter p_α obeys the inequality:

$$\langle \Delta p_\alpha^2 \rangle \geq (\mathbf{F}^{-1})_{\alpha\alpha}, \quad (11)$$

where (\mathbf{F}^{-1}) denotes the inverse of the Fisher matrix and Δp_α is the relative error on parameter p_α around its fiducial value, including marginalization over the other parameters.

This formalism has been used to forecast constraints on the dark energy density Ω_{de} and equation of state parameters w_0 and w_a . Lensing is also sensitive to other cosmological parameters that affect either the primordial power spectrum or the growth of structure (49, 45, 40). Since the projected power spectrum probed by lensing is a slowly varying function of wavenumber (unlike the CMB), it is not sensitive to parameters that produce localized features such as the baryon mass fraction. However its shape can help constrain neutrino masses and a running spectral index. Lensing tomography is most sensitive to variables that affect the amplitude at different redshift: this is what gives the greatest leverage on dark energy parameters. Thus the use of all the auto and cross-spectra that can be measured with redshift information is critical in extracting cosmological information from lensing.

Figure 3 shows dark energy forecasts obtained for a 5000 deg² Stage III experiment (in the terminology of the Dark Energy Task Force (6)), with all other relevant cosmological parameters marginalized over (40). CMB priors are used, at the level of the Planck experiment. Statistical errors due to sample variance

and finite intrinsic ellipticity are included, but the effect of systematic errors is not: those are discussed and estimated in §4 below. Aside from the issue of systematics, forecasts for lensing are still challenging because there are multiple observables (power spectra, bispectra, cluster counts). These observables are not independent, and much of the information is in the non-Gaussian regime which makes the estimation of covariances difficult. In Figure 3 we have used power spectra and bispectra in three broad redshift bins, and included covariances based on the halo model (Takada & Jain, in preparation).

4 Systematic errors

Weak lensing measurements are prone to a number of systematic errors. The first category of systematics arise in the measurement of galaxy shapes. But there are others that enter in the estimation of cosmological parameters given a galaxy shape catalog. The primary sources of systematic error can be characterized as:

- Knowledge of the PSF
- Correction of the PSF and shear calibration
- Intrinsic alignments
- Photometric redshifts
- Non-linear power spectrum/effect of baryons

While each of these errors is well studied and can be modeled, small residuals in the corrections of these errors may well be comparable to statistical errors in lensing measurements. The first two sources of error follow directly from our discussion in §2 of lensing shape measurements. The remaining systematics become important if we wish to interpret the lensing signal and compare it with a cosmological model.

Intrinsic alignments are caused by the tidal gravitational field, which can cause the shape of a galaxy to be aligned with another due to direct interactions. It is currently the least well characterized source of systematic error in lensing. Photo- z uncertainties can contribute to systematic errors because the cosmological inferences of lensing measurements depend sensitively on the estimated photo- z . Finally, the theoretical model predictions may have uncertainties due to nonlinear gravitational clustering and baryonic gas physics that affect the lensing power spectrum. Another complication is the fact that we do not observe the shear directly, but the reduced shear $\gamma/(1 + \kappa)$ instead. We discuss the systematic errors due to intrinsic alignments below, as these are the least well characterized at present.

4.1 Intrinsic alignments

Thus far we have assumed that the galaxy ellipticities are uncorrelated in the absence of lensing. However, there are reasons to believe that this assumption

is not valid and that intrinsic alignments in the galaxy shapes contaminate the lensing signal. Two kinds of intrinsic alignment effects have been identified. Before we discuss these in more detail, we note that relatively little is known about this effect, except that the alignments are relatively small. It is safe to say that currently a robust measurement of this signal is almost as difficult as that of the cosmic shear signal itself.

The first type to be identified is due to alignments of galaxy halos with other halos that respond to tidal gravitational forces. Early work based on simulations and analytic models (50,28) demonstrated how this process can compromise cosmic shear measurements. There is, however, considerable theoretical uncertainty in modeling the alignment of halos themselves, and how well the luminous matter (that is observed) aligns with the dark matter. Importantly, this source of systematics can be greatly reduced with photo-z's by using cross-spectra of galaxies in two different redshift bins (so that galaxy pairs are separated by large distances at which the tidal effects are very weak).

The second alignment effect was pointed out by (51). It arises from the fact that the shapes of galaxies may be correlated with their surrounding density field. This field is also responsible for the weak lensing shear. As a result an anti-correlation between the shapes of galaxies at different redshifts is introduced, leading to a suppression of the lensing signal. While the first intrinsic alignment effect can be minimized by using galaxies at different redshifts in shear correlation measurements, this second mechanism affects pairs of galaxies at different redshifts. Without further theoretical and observational progress, therefore, the two classes of intrinsic alignments can be a very difficult systematic to overcome and can bias cosmic shear results (e.g., (52)). Fortunately some handle on the level of these effects is now available thanks to spectroscopic data (53,54) and theoretical progress via numerical simulations is also being made (55). Nonetheless, as shown by (52), intrinsic alignments need to be taken into account when designing future surveys as they affect the requirements on the accuracy of photo-z's.

4.2 How systematics degrade cosmological constraints

A comprehensive study of lensing systematics can be made with the following general expression of the estimated shear (48):

$$\hat{\gamma}(z_s, \mathbf{n}) = \gamma_{lens}(z_s, \mathbf{n}) [1 + \gamma_{sys}^{mult}(z_s, \mathbf{n})] + \gamma_{sys}^{add}(z_s, \mathbf{n}) \quad (12)$$

The above equation includes two kinds of systematic error contributions, which modify the lensing shear via additive and multiplicative terms. In addition, the bin redshift z_s and its width may also be in error, leading to biases in cosmological parameters (56).

Two key points in understanding the degradation of cosmological information due to systematics are: (i) The impact of systematics on shear correlations is what matters, e.g. errors that affect individual galaxy shapes but are uncorrelated

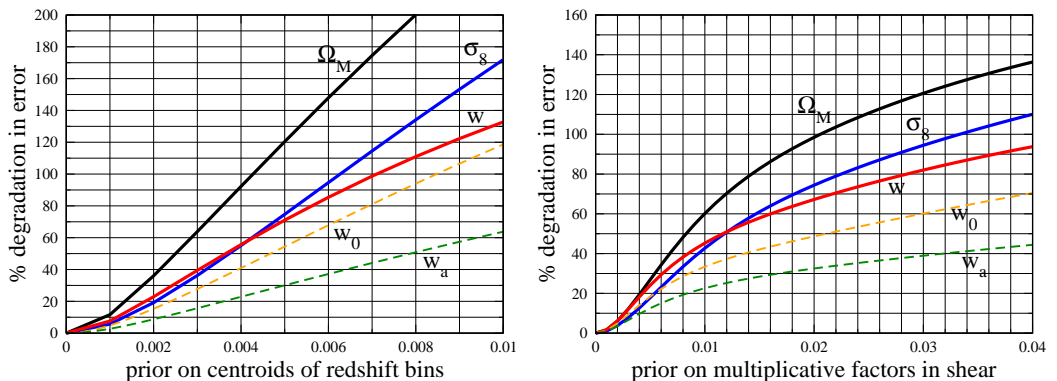


Figure 4: Degradation in cosmological parameter accuracy due to systematic errors (48). The left panel shows the effect of biases in photo- z 's for a Stage III survey. The right panel shows the effect of shear calibration errors. There is some evidence for a self-calibration regime for these, unlike for photo- z biases. Note that only the fractional degradation in parameter accuracy is shown here.

between galaxy pairs simply act as additional statistical errors (and are likely to be subdominant to the intrinsic shape noise of galaxies). (ii) Systematic errors typically do not share the full redshift dependence of the lensing signal. For example, errors in shear calibration may depend on galaxy size and brightness, but not directly on redshift. This allows us to fit for uncertainty in the shear calibration from the data. In general, by using all available auto- and cross-spectra, one can marginalize over a set of systematic error parameters. (The exception is photo- z biases, which can mimic the cosmological signal and must be controlled with an appropriate calibration sample.)

Figure 4 shows how two of these systematic errors degrade cosmological parameter accuracy: shear calibration errors and photo- z biases. The right panel in this figure shows the possibility of self-calibration: the degradation plateaus somewhat, because the redshift dependence of the lensing signal allows for joint measurements of parameters describing both systematics (shear calibration in this case) and cosmology. The modeling and reduction of systematics is an area of active study (e.g. (57)). The degradation estimates shown in Figure 4 are meant to be conservative in that no assumptions are made about the functional forms of these systematics and only the shear power spectra are used.

In summary, progress in handling systematic errors is being made on several fronts: for PSF effects, in the use of improved algorithms; for photo- z 's, in the use of large calibration samples; for intrinsic alignments, via new measurements as well as physical models; and for predictions in the nonlinear regime, from N -body and hydrodynamical simulations. The scientific returns of planned surveys rely on continued advances in these directions.

Table 1: Overview of recent surveys. The survey size and inferred value of σ_8 and w (where available) are shown for the large ground based surveys and the largest spaced based survey. The σ_8 values are quoted at fixed Ω_m to check the consistency of the measured lensing amplitude in different surveys. Meaningful confidence intervals on σ_8 require a joint analysis with CMB data (see text in §5.1). Further, since these studies have dealt with marginalization and systematic errors in different ways, direct comparisons are difficult.

Survey	Area [deg ²]	Ref.	σ_8 ($\Omega_m = 0.3$)	w	Ref.
RCS	53	(62)	0.65 ± 0.07		(72)
VIRMOS	8.5	(63)	0.83 ± 0.06		(72)
CTIO ^a	70	(64)	$0.81^{+0.15}_{-0.10}$	$-0.89^{+0.16}_{-0.21}$	(64)
GaBoDS	13	(65)	0.78 ± 0.08		(72)
CFHTLS ^{b,c}	57	(66)	0.71 ± 0.04	< -0.5	(66)
COSMOS	2	(67)	$0.87^{+0.09}_{-0.7}$		(67)

^a: error bars correspond to 95% confidence limits and are joint constraints using WMAP priors;

^b: published analyses do not include full area and are based on i' data only. The completed survey will image 140 square degrees in 5 filters; ^c: the upper limit on w is from (68)

5 Observational results

The advent of wide field imaging cameras on 4m class telescopes in the late 1990s made the first cosmic shear detections possible (58, 59, 60, 61). Since then, the size of weak lensing surveys has increased significantly, and current surveys have imaged several tens of square degrees of the sky. An extensive list of early work can be found in (10), but here we limit the discussion to the relatively large surveys listed in Table 1. We only include references to the most up-to-date analyses, which include a separation of the signal into ‘E’ and ‘B’-modes. The results listed in Table 1 all find small or negligible ‘B’-modes, in particular on scales larger than a few arcminutes. Furthermore, the lensing pipelines used to obtain these measurements are amongst the most accurate ones available (see §2.4 and (16, 17)). The cosmological measurements from these surveys are discussed below in §5.1.

Constraints on cosmological parameters have not improved dramatically, because of the limited knowledge of the source redshifts. The ability to measure the growth of structure as a function of redshift will be the next major leap forward for cosmic shear studies. The first steps in that direction have already been taken and the bottom three surveys in Table 1 are able to derive photometric

redshifts for the sources thanks to their multi-color data¹. The first tomographic results have already been presented (69, 67), albeit based on small areas which leave them susceptible to non-Gaussian contributions to the sample variance. The COSMOS survey combines the excellent image quality of the Hubble Space Telescope with an extensive follow-up campaign to map the three-dimensional large scale structure (70) and measure the cosmic shear signal as a function of redshift (67). Expanding space based observations beyond the COSMOS survey area will require a dedicated space based mission (see §7); ground based surveys will lead the way in the near future.

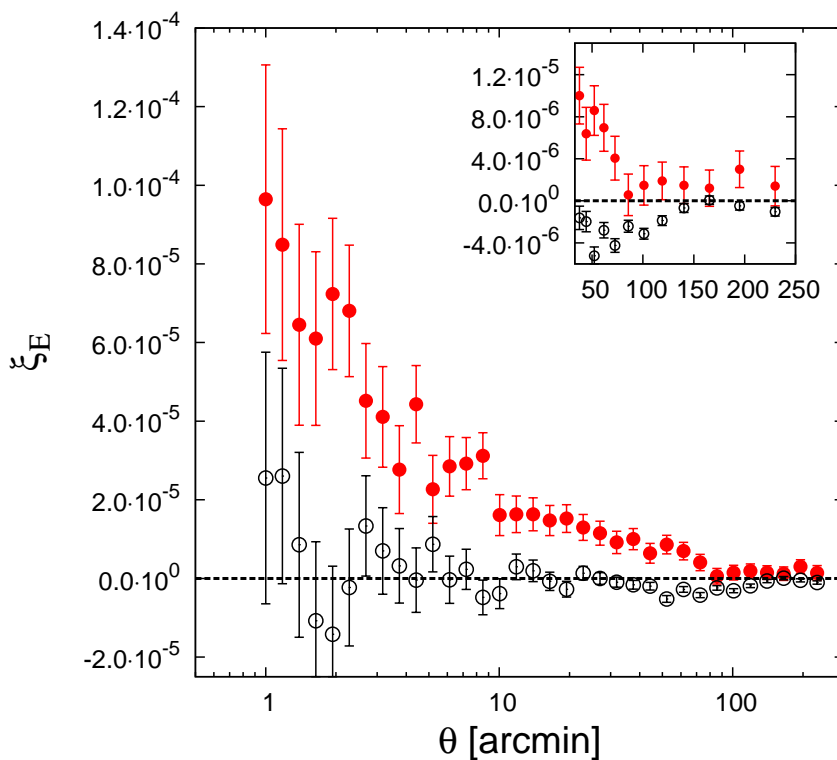


Figure 5: Ellipticity correlation function from (66). These measurements based on the analysis of 57 deg² of CFHTLS *i'* imaging data, extend out to 4 degrees, well into the linear regime. The E-modes are indicated by the red points. The B-mode (open points) is consistent with zero on most scales. As shown in the enlargement, there is an indication of residual systematics on a scale of one degree, which corresponds to the size of the camera.

Canada-France-Hawaii-Telescope Legacy Survey: The CFHTLS is the largest cosmic shear survey carried out to date. Once completed, by the beginning of 2009, it will have imaged 140 square degrees in the five Sloan filters, and

¹A fourth survey, the Deep Lens Survey, has also collected multi-color data, but no recent results have been published

galaxies as faint as $i' = 24.5$ are included in the analysis. The availability of photometric redshifts for the sources will improve the constraints on cosmological parameters significantly. The goal of the completed survey is to constrain w with a relative accuracy of 5 – 10%.

The first results, based on a conservative analysis of the first year i' data were presented in (68), whereas (71) measured the signal from the “deep” component of the survey. More recently, (66) analysed 57 deg² of CFHTLS i' . As shown in Figure 5, (66) were able to measure the lensing signal out to 4 degrees, well into the linear regime.

5.1 Implications for cosmology

As discussed above, our limited knowledge of source redshifts is still a significant source of uncertainty in many lensing studies. This situation is improving rapidly, however, thanks to multi-color surveys such as COMBO-17, COSMOS and CFHTLS. This has led to an updated analysis of the RCS (62), VIRMOS (63), the Garching-Bonn Deep Survey (GaBoDS;(65)) and first year CFHTLS (68) measurements by (72). Compared to the original measurements, (72) include a more sophisticated treatment of the sample variance errors on small scales, as suggested by (73). The new analyses also include, where necessary, corrections to the signal based on the STEP results (16,17). Most importantly, they use up-to-date redshift distributions for the surveys based on the large photometric redshift catalog published by (74).

Due to the lack of tomographic measurements most lensing results only constrain a combination of Ω_m and σ_8 . This is demonstrated clearly in Figure 6, which shows in purple the weak lensing results from (66). The various estimates for σ_8 are listed in Table 1 (adopting a Λ CDM cosmology with $\Omega_m = 0.3$ for reference, except for (64) who have marginalized over all parameters in combination with CMB data). The ensemble averaged value for σ_8 (adopting $\Omega_m = 0.3$) from these recent measurements is $\sigma_8 = 0.75 \pm 0.03$ with a $\chi^2 = 7.4$ with 5 degrees of freedom. The agreement between these results is therefore reasonable (the probability of a larger χ^2 is 0.19). We note, however, that this statistical error ignores any common systematics.

As shown in Figure 6 the combination of lensing and CMB measurements is useful in constraining Ω_m and σ_8 . This joint analysis from (66) with the WMAP3 results (77) yields $\Omega_m = 0.248 \pm 0.019$ and $\sigma_8 = 0.771 \pm 0.029$. These are fully consistent with the previous lensing based analysis from the CTIO survey of (64). These results are also in agreement with recent studies of the number density of clusters of galaxies (e.g., (75, 76); also see (65) for a compilation of recent measurements). Measurements of w , the dark energy equation of state, are still limited due to the lack of tomographic results from large area surveys, but two tentative results from analyses with constant w are listed in Table 1.

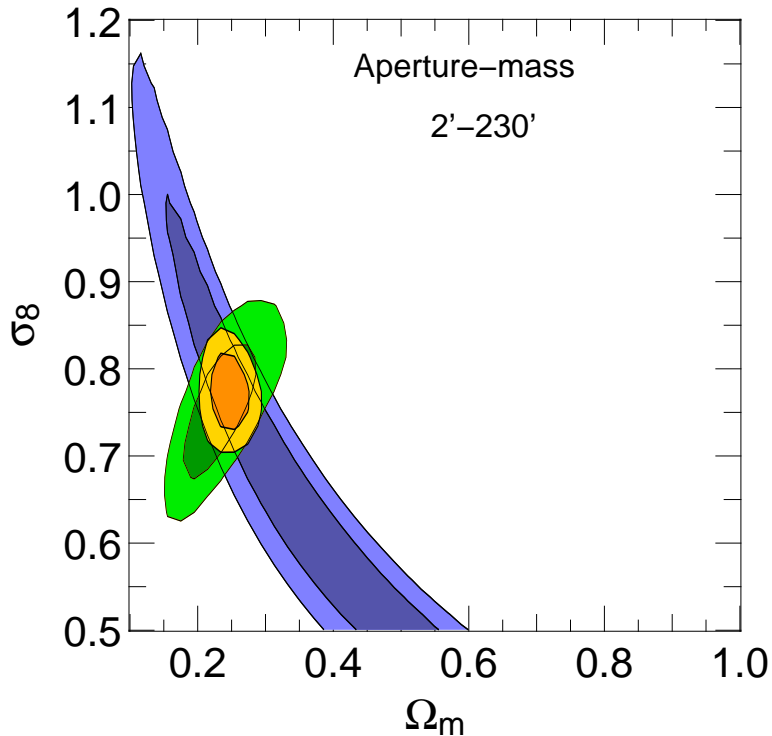


Figure 6: Joint constraints on Ω_m and σ_8 from the CFHTLS (66) (purple) and WMAP3 (77) (green). The CFHTLS results are based on the aperture mass statistic on scales ranging from $2' - 230'$. The combined constraints from weak lensing and CMB are indicated by the orange region, demonstrating excellent agreement. Also note the complementarity of lensing to CMB observations.

6 Lensing by galaxies and galaxy clusters

The study of cosmic shear has been the main science driver of most recent weak lensing studies, but in this section we highlight some of the applications to galaxy and cluster lensing which pertain to cosmology and the study of dark matter.

6.1 Mapping the distribution of dark matter

The observed weak lensing shear field provides estimates of the derivatives of the lensing potential (see Eqn. 5). As shown by (78) it is possible to invert this problem to obtain a parameter-free reconstruction of the surface density distribution: it is possible to make an ‘image’ of the dark matter distribution. The surface density (up to an arbitrary constant κ_0) can be written as (78):

$$\kappa(\boldsymbol{\theta}) - \kappa_0 = \frac{1}{\pi} \int d^2\boldsymbol{\theta}' \frac{\zeta(\boldsymbol{\theta}' - \boldsymbol{\theta})\gamma(\boldsymbol{\theta}')}{(\boldsymbol{\theta}' - \boldsymbol{\theta})^2}, \quad (13)$$

where the convolution kernel $\zeta(\boldsymbol{\theta})$ is given by

$$\zeta(\boldsymbol{\theta}) = \frac{\theta_2^2 - \theta_1^2 + 2i\theta_1\theta_2}{|\boldsymbol{\theta}|^4}. \quad (14)$$

The proper evaluation of this integral requires data out to infinity, which is impractical. This complication spurred the development of finite-field inversion methods (79, 80, 81).

The intrinsic shapes of the sources add significant noise to the reconstruction and as a result only the distribution of matter in massive clusters of galaxies can be studied in detail using weak lensing mass reconstructions. Of particular interest is the study of merging systems, where dynamical techniques cannot be used (1, 82, 83). Figure 7 shows a reconstruction of the mass distribution of the Bullet cluster by (1) based on HST observations. The reconstructed (dark) matter distribution is offset from the hot X-ray gas, but agrees well with the distribution of galaxies. As shown by (1), these observations provide some of the best evidence for the existence of dark matter (also see the discussion in (84)). This is because in alternative theories of gravity (such as Modified Newtonian Dynamics (85, 86)) the hot X-ray gas should be the main source of the lensing signal. In the near future we can expect improved constraints on the properties of dark matter particles based on a systematic study of merging systems.

6.2 Cosmology with galaxy clusters

Since clusters trace the highest peaks in the density, their number density as a function of mass and redshift depends strongly on the underlying cosmology (e.g., (76, 87)), making it an interesting complementary probe for dark energy studies (e.g., (88)). Although conceptually straightforward, the implementation of this method has proven difficult.

One reason is that precise measurements of cosmological parameters require cluster catalogs with well-defined selection functions. In principle clusters can be identified in mass reconstructions from large weak lensing surveys (e.g., (89, 90, 91)), but projections along the line-of-sight lead to a relatively high false positive rate (e.g., (92, 93)). Hence, either one must work with a statistic that includes projection effects (e.g. (94)), or with samples derived from optical, X-ray or radio observations.

Even in the latter case it is essential to have a well-determined relation between the observed cluster properties and mass. This is where weak lensing studies of large cluster samples can play an important role. The determination of the mean relation between the quantity of interest (e.g., richness, X-ray temperature) and cluster mass can be done statistically. For instance, (95, 96) have measured the ensemble averaged weak lensing signal as a function of richness and luminosity using data from Sloan Digital Sky Survey (SDSS). Unfortunately, the mass-observable is expected to have an intrinsic scatter as well, which is the result of differences in formation history, etc. The precise characterization of this unknown scatter is important to ensure accurate measurements of cosmological

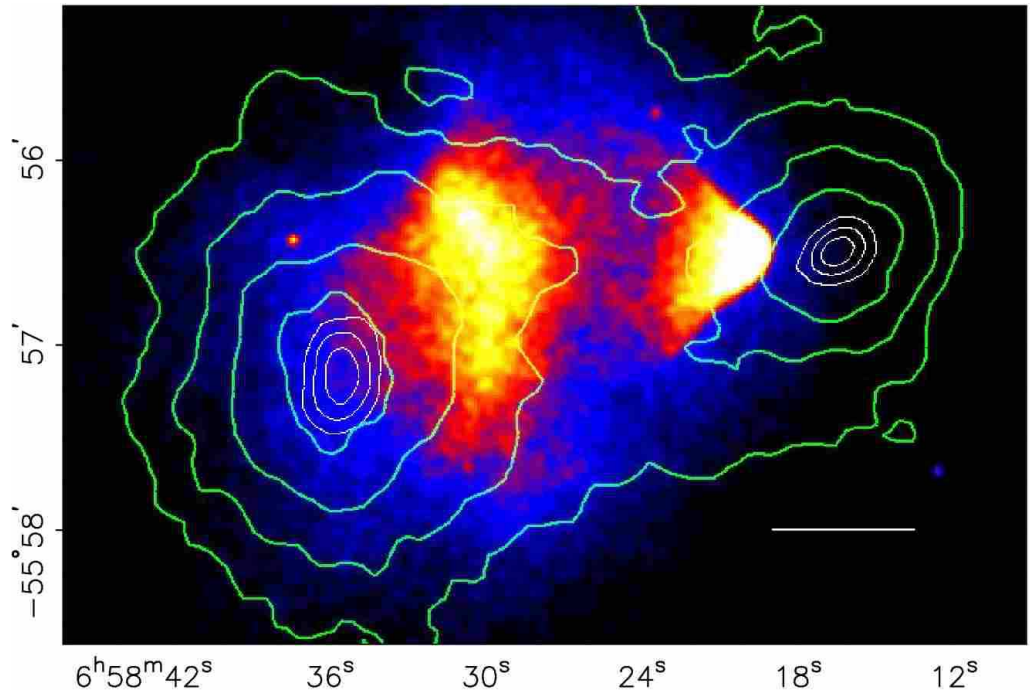


Figure 7: X-ray emission from the ‘Bullet’ cluster of galaxies as observed by Chandra. The eponymous bullet is a small galaxy cluster which has passed through the larger cluster and whose hot gas is seen in X-rays as the triangular shape on the right. The contours correspond to the mass reconstruction from (1). The dark matter distribution is clearly offset from the gas, which contains the majority of baryonic matter, but agrees well with the distribution of galaxies – as expected if both the dark matter and stars in galaxies are effectively collisionless. See (1) for a complete discussion of this intriguing object.

parameters. Individual weak lensing masses can be derived for massive clusters. We note, however, that ultimately the accuracy of these mass measurements is limited by projections along the line of sight (97,98,99,92).

Multi-wavelength observations of samples that contain up to ~ 50 massive clusters have only recently started (100,101,102). These comprehensive studies, which also combine data at other wavelengths, will not only help quantify the scatter, but will also improve our understanding of cluster physics. This in turn will increase the reliability of other cluster mass estimators (such as the X-ray temperature). For instance, recently (103), found evidence that the outer regions of clusters are not in hydrostatic equilibrium, suggesting that additional pressure may be provided by bulk motion of the plasma (104). Cluster cosmology is an evolving field, and the hope is that with large samples of clusters observed in multiple wavelengths their internal physics will be modeled well enough for cosmological applications.

6.3 Properties of dark matter halos

Simulations of hierarchical structure formation in CDM cosmologies have shown that the density profiles of virialized halos over a wide range in mass have a nearly universal profile with radius – the Navarro-Frenk-White (NFW) profile (105,106). The only difference between halos of galaxies and clusters of different mass is their concentration, which reflects the central density of the halo. Gravitational lensing provides us with powerful tools to test a range of predictions of the CDM paradigm via the structure of halos. For instance, the dark matter dominated outer regions can be uniquely probed by weak lensing, whereas strong gravitational lensing can be used to study the density profile on small scales.

Central regions: In the context of CDM, simulations indicate a power law density profile $\rho \propto r^{-\beta}$ as $r \rightarrow 0$. The original studies (105,106) found a slope of $\beta = 1$, but the exact value is still debated (107,108). Without a complete treatment of the effects of baryons, observational results will be difficult to interpret. Despite these complications, much effort is devoted to determine the slope of the density profile observationally, as it can provide unique constraints on physical properties of the dark matter particle, such as its interaction cross section (e.g. (109,110)).

Dynamical studies of galaxies have proven useful, and much of the current controversy about the central slope is based on observations of the rotation curves of low surface brightness galaxies, which suggest that the dark matter distribution has a central core (e.g.,(111,112,113)). Strong lensing by galaxies can provide limited information because the typical Einstein radius is large compared to the region of interest. Nevertheless, the combination of strong lensing and dynamics has shown to be extremely useful for the study of the stars and dark matter in galaxies (e.g., (114,115)) and to test general relativity (116).

Strong lensing can be used to study the inner density profiles of clusters, although results are still somewhat ambiguous (117). Of particular interest are clusters that show both tangential and radial arcs, because these can help to constrain the density profile. An analysis of such systems by (118) suggests an average slope $\beta \sim 0.5$. However, (119) studied simulated clusters and found that too restrictive assumptions can bias core slope estimates to lower values (also see (120,121)).

Outer regions: The value for the outer slope of the density profile is expected to be $\beta \sim 3$. A related prediction is that the mean central density of the halo decreases with virial mass, i.e., lower mass systems are more concentrated (105,106). The average dark matter profile of galaxy clusters has been studied by (96) using SDSS. These results and measurements by (122,123) agree well with predictions from Λ CDM models, as do studies of individual clusters such as Abell 1689(124).

The study of the outer parts of galaxies is more difficult, because the signal

of an individual galaxy is too small to be detected. The interpretation of the observed signal, also known as the galaxy-mass cross-correlation function (e.g., (125,126,46)) is complicated by the fact that it is the convolution of the galaxy dark matter profile and the (clustered) distribution of galaxies. Despite these limitations, galaxy-galaxy lensing studies provide a number of useful tests of the cold dark matter paradigm.

One such test is the measurement of the extent of dark matter halos. Pioneering studies by (127,128) were unable to provide constraints because of the small numbers of lens-source pairs. Large surveys, such as SDSS (e.g., (129,126,130)), RCS (125) and CFHTLS (131) have measured the lensing signal with much higher precision, enabling (125) to determine the extent of dark matter halos around field galaxies. Note that these measurements use the small scale end of the galaxy-shear cross-correlation discussed above in §3.2.

Another area where galaxy-galaxy lensing studies will have a great impact is the study of the shapes of dark matter halos. CDM simulations predict that halos are tri-axial (e.g (132)). This is supported by the findings from (125), who found that the dark matter halos are on average aligned with the light distribution with a mean axis ratio that is in broad agreement with the CDM predictions. A similar result was obtained recently by (131) using CFHTLS data. Both these studies lacked the multi-color data to separate lenses by galaxy type. Such a separation was done by (133) using SDSS data. They did not detect a significant flattening, although their data do suggest a positive alignment for the brightest ellipticals.

The accuracy of these measurements is expected to improve significantly over the next few years as more data is collected as part of cosmic shear surveys. An accurate measurement of the anisotropy of the lensing signal around galaxies (i.e, the signal of flattened halos in CDM) is also a powerful way to test alternative theories of gravity (134,125).

7 The Future

The first cosmic shear results, published less than a decade ago, were based on areas of several square degrees at most (58,59,60,61). Current leading surveys, most notably the CFHTLS, are many times larger and provide photometric redshift information for the sources. Even so, the area coverage of CFHTLS is still modest (below 200 deg²) given that it is now technologically feasible to image more than a thousand square degrees per year to depths of interest for cosmology. Furthermore, despite the recent success in measuring the cosmic shear signal, current data are obtained using telescopes that are not optimized for weak lensing. Finally, the use of photo-z's for cosmological inferences is still in its early stages. The CFHTLS lacks good coverage at near-infrared wavelengths, which impacts the accuracy of photo-z's.

Table 2: Overview of planned surveys

Survey	Start	Area [deg ²]	n_{eff} [arcmin ⁻²]	Ground/Space
KiDS	> 2008	1500	~ 10	ground
PanSTARRS ^a	> 2008	30,000	~ 4	ground
DES	> 2010	5000	~ 10	ground
Subaru	> 2012	2000	$\sim 20\text{-}30$	ground
LSST	> 2014	20,000	$\sim 30\text{-}40$	ground
SNAP	> 2015	4000	~ 100	space
DUNE	> 2015	20,000	~ 40	space

^a Here we consider PS1, the PanSTARRS project with a single telescope and the 3π survey.

We note that this project may be expanded into a four telescope project in subsequent years (referred to as PS4).

7.1 Planned surveys

The next generation of surveys will address some or even all of these limitations. For instance, many will make use of new telescopes specifically designed to provide a stable PSF with minimal anisotropy. Equipped with new cameras with fields of view of a square degree or larger, these surveys will deliver over 1000 deg² of well calibrated images of galaxies beyond $z = 1$. Table 2 lists some basic information for a number of these projects. As many of these surveys are still in the planning stage, we stress that these numbers may change. Experience shows that this is particularly true for the starting dates! What is clear from this table is that the data size will increase by another order of magnitude in approximately the next five years.

Of the first four surveys listed in Table 2, the Kilo Degree Survey² (KiDS) and the Panoramic Survey Telescope and Rapid Response System³ (PanSTARRS) use telescopes and cameras specifically designed for the projects. The Dark Energy Survey⁴ (DES) will use a new camera built for the 4m Blanco telescope at CTIO. Similarly, a new camera, the HyperSuprimeCam, has been proposed for the Subaru 8.2m telescope. KiDS will use near-infrared imaging with the VISTA telescope; the resulting 9-band data will give it excellent photometric redshift accuracy, which is critical for the measurement of intrinsic alignments and cosmic shear tomography. DES also plans to use near-IR imaging over a substantial part of the survey.

The accuracy with which the lensing signal can be measured depends on the

²<http://www.strw.leidenuniv.nl/~kuijken/KIDS/>

³<http://pan-starrs.ifa.hawaii.edu>

⁴<http://www.darkenergysurvey.org>

area covered and the number density of distant source galaxies for which reliable shapes and photo-z's can be determined. For a fixed amount of observing time, one therefore has to strike a balance between the amount of sky covered and the depth of the observations. If the survey is too shallow, most sources will be at low redshift, and the induced lensing signal will be too small to be of interest.

On the other hand, increasing the number density of sources used in the analysis is useful only if systematic effects for these small, faint galaxies can be controlled or corrected for. The blurring of the images by the atmosphere is a limiting factor. If the size of the galaxy is comparable to that of the PSF, any residual systematic is amplified by the “deconvolution”. Compared to space based observations, ground based observations are therefore more sensitive to problems with PSF correction. Furthermore, obtaining deep near infrared (NIR) data, needed for accurate photometric redshifts, will be more difficult for a ground based telescope (though it would be feasible to add imaging in these bands from space provided the depth and sky coverage match).

Much of the cosmological information in planned surveys is extracted from large scale modes, for which sample variance is the limiting factor, not the number density. Consequently, ground based surveys may suffer only a modest loss of accuracy if only galaxies with well measured shapes and photo-z's are used. Further, the cost of a space based project requires a careful consideration of the benefits. While many of these considerations are being worked on, it is clear that the requirements to reach percent level accuracy in the dark energy equation of state are very challenging.

In Table 2 we provide crude estimates for the expected effective source number densities for the various surveys. These numbers could change depending on the delivered seeing and noise levels for a given survey. We note that due to PSF degradation effects, the effective number density of sources that can be used in the lensing analysis, n_{eff} , is lower than the number density of detected objects. Studies based on simulated and actual deep ground based images suggest that it is difficult to exceed an effective density of 30 galaxies arcmin⁻² in typical ground based data (this upper limit depends on the seeing and other factors). A space based mission is required to reach significantly higher source densities.

The projects that will start in the immediate future represent a major step forward, but they will be carried out on mostly general purpose facilities (with the exception of PanSTARRS). This limits the amount of time available for large multi-wavelength surveys. Hence, a significantly larger, deep survey would require a dedicated large aperture telescope with a very wide field-of-view. One proposal is the expansion of PanSTARRS to include more telescopes to increase the etendue (field-of-view times collecting area) of the facility. A proposal for arguably the definitive ground-based survey is the 6-band imaging survey over 20,000 square degrees proposed for the Large Synoptic Survey Telescope⁵ (LSST), an 8.4m telescope with a 10 square degree field of view whose survey capacity is

⁵<http://www.lsst.org>

an order of magnitude larger than any Stage III project.

Alternatively, in an attempt to minimize PSF related systematics, space based missions are being planned. These have the added benefit that high quality multi-wavelength data out to NIR wavelengths can be obtained. A European project, the Dark UNiverse Explorer⁶ (DUNE) focuses on the improved image quality and stability that can be obtained from space, but, in its current form, still relies on extensive ground based follow-up. Also, the improvement in n_{eff} is relatively small compared to LSST. The SuperNova/Acceleration Probe⁷ (SNAP) is the most comprehensive proposal, as it combines stable optics for weak lensing shape measurements with 9-filter optical/NIR photometry for superb photometric redshifts. It will survey a smaller area of the sky than DUNE, but to a greater depth.

7.2 Prospects for lensing cosmology

This review has covered weak lensing by galaxies, galaxy clusters and large-scale structure. We have discussed the measurement of cosmological parameters via lensing, with a focus on dark matter and dark energy. The use of lensing tomography for dark energy measurements can be performed using (two- and three-point) shear correlations, galaxy-shear cross-correlations and galaxy clusters. Tests of the nature of dark matter and of gravity on scales of 10 kpc to 1 Mpc are provided by galaxy and cluster lensing. Modified gravity theories that attempt to explain the cosmic acceleration can also be tested using weak lensing measurements on larger (cosmological) scales. The success of particular applications of lensing will no doubt depend on how well systematic errors can be reduced, corrected from the data or marginalized over in making cosmological inferences.

Most weak lensing studies (and therefore this review) have focused on the measurement of the shear using galaxy images. These studies will continue to provide unique insights in the dark side of the universe. In conclusion, we highlight a few other aspects of lensing that are the subject of ongoing research. For instance, the lensing signal can also be inferred by measuring magnification effects which change the number counts of source galaxies (135, 136). These effects can provide a useful complementary measure of lensing as the systematic errors involved are quite different from shear measurements. We mentioned three-point shear correlations as useful measures of the non-Gaussian distribution of the lensing mass. Other measures of non-Gaussianity include global characterization of the topology of lensing maps, topological charge distributions, peak statistics in convergence maps and so on.

We also discussed the binning of galaxies using photo- z 's for lensing tomography. It is possible to do better and treat the source galaxy distribution as three-dimensional (with the position in the redshift direction having much larger

⁶<http://www.dune-mission.net>

⁷<http://snap.lbl.gov>

uncertainty than in the transverse direction), which can lead to improved cosmological constraints (137). Another application of tomography is the actual reconstruction of the three-dimensional lensing mass distribution (138, 139); an attempt has been made using the COSMOS survey carried out with the HST (70). A relatively new area of research is the measurement of higher order derivatives of the lensing potential, which provide additional information on small scale variations in the mass distribution (140, 141).

Finally, we mention two high redshift applications of lensing. An area of active study is the effect of lensing by foreground structures on the CMB (142, 143). This is a significant contaminant for studies of the CMB polarization (144), but can also provide additional information about the lensing mass. Finally, future radio telescopes may be able to detect galaxies at high redshift through their 21cm emission. If lensing effects can be measured accurately with 21cm surveys, they can provide high accuracy power spectra over a wide range in redshift (145, 146, 147).

Acknowledgement. We acknowledge helpful discussions and comments on the manuscript from Gary Bernstein, Jacek Guzik, Mike Jarvis, Nick Kaiser, Steve Kahn, Eric Linder, Jason Rhodes, Alexandre Refregier, Fritz Stabenau, Masahiro Takada, Andy Taylor and Ludo van Waerbeke. This work is supported in part by the Department of Energy, the Research Corporation and NSF grant AST-0607667.

LITERATURE CITED

1. Clowe D, Bradac M, Gonzalez AH, Markevitch M, Randall SW, Jones C, Zaritski D *Astrophys. J.* 648:L109 (2006)
2. Refsdal S *MNRAS* 128:307 (1964)
3. Koopmans LVE, Treu T, Fassnacht CD, Blandford RD, Surpi G *Astrophys. J.* 599:70 (2003)
4. Blandford RD, Saust AN, Brainderd TG, Villumsen JV *MNRAS* 251:600 (1991)
5. Kaiser N *Astrophys. J.* 388:272 (1992)
6. Albrecht A, et al. “*Report of the Dark Energy Task Force*” arXiv:astro-ph/0609591 (2006)
7. Peacock JA et al. *ESA-ESO Working Group on "Fundamental Cosmology"* arXiv:astro-ph/0610906 (2006)
8. Bartelmann M, Schneider P arXiv:astro-ph/9912508 (1999)
9. Mellier Y *Annu. Rev. Astron. Astrophys* 37:127 (1999)

10. Refregier A *Annu. Rev. Astron. Astrophys.* 41:645 (2003)
11. Munshi D, Valageas P, van Waerbeke L, Heavens A arXiv:astro-ph/0612667 (2006)
12. Seitz C, Schneider P *Astron. Astrophys* 318:687 (1997)
13. Jain B, Jarvis M, Bernstein G *JCAP* 2:1 (2006)
14. Hoekstra H. *MNRAS* 347:1337 (2004)
15. Jarvis M, Jain B. arXiv:astro-ph/0412234 (2004)
16. Heymans C, et al. *MNRAS* 368:1323 (2006)
17. Massey R, et al. *MNRAS* 376:13 (2007)
18. Kaiser N, Squires G, Broadhurst T *Astrophys. J.* 449:460 (1995)
19. Luppino GA, Kaiser N *Astrophys. J.* 475:20 (1997)
20. Hoekstra H, Franx M, Kuijken K, Squires G *Astrophys. J.* 504:636 (1998)
21. Bernstein GM, Jarvis M *Astron. J.* 123:583 (2002)
22. Refregier A *MNRAS* 338:35 (2003a)
23. Refregier A, Bacon D *MNRAS* 338:48 (2003)
24. Nakajima R, Bernstein G *Astron. J.* 133:1763 (2007)
25. Kuijken K *Astron. Astrophys* 352:355 (1999)
26. Bacon DJ, Massey RJ, Refregier AR, Ellis RS *MNRAS* 344:673 (2003)
27. Schneider P, van Waerbeke L, Mellier Y *Astron. Astrophys* 389:729 (2002)
28. Crittenden RG, Natarajan P, Pen U-L, Theuns T *Astrophys. J.* 559:552 (2001)
29. Hu W *Astrophys. Journal*, 522:L21 (1999)
30. Knox L, Song Y-S, Tyson JA *Phys. Rev. D* 74:023512 (2006)
31. Amendola L, Kunz M, Sapone D arXiv:0704.2421 (2007)
32. Jain B, Zhang P arXiv:0709.2375 (2007)
33. Heavens AF, Kitching TD, Verde L *MNRAS* 380:1029 (2007)
34. Huterer D, Linder EV *Phys. Rev. D* 75:023519 (2007)
35. Jain B, Seljak U *Astrophys. J.* 484:560 (1997)
36. Jain B, Seljak U, White S *Astrophys. J.* 530:547 (2000)
37. White M, Vale C *Astroparticle Physics* 22:19 (2004)
38. Francis MJ, Lewis GF, Linder EV *MNRAS* 380:1079 (2007)
39. Zentner AR, Rudd DH, Hu W arXiv:0709.4029 (2007)
40. Takada M, Jain B *MNRAS* 348:897 (2004)

41. Hu W, Jain B *Phys. Rev. D* 70:043009 (2004)
42. Jain B, Taylor A *Phys. Rev. Lett.* 91:141302 (2003)
43. Bernstein G, Jain B *Astrophys. J.* 600:17 (2004)
44. Zhang J, Hui L, Stebbins A *Astrophys. J.* 635:806 (2005)
45. Song YS, Knox L *Phys. Rev. D* 70:063510 (2004)
46. Seljak U, et al. *Phys Rev D* 71:043511 (2005)
47. Bernardeau F, van Waerbeke L, Mellier Y *Astron. Astrophys.* 322:1 (1997)
48. Huterer D, Takada M, Bernstein G, Jain B *MNRAS* 366:101 (2006)
49. Hu W, Tegmark M *Astrophys. J.* 514:L65 (1999)
50. Croft RAC, Metzler CA *Astrophys. J.* 545:561 (2000)
51. Hirata C M, Seljak U *Phys. Rev. D* 70:063526 (2004)
52. Bridle S, King L *NJP* 9:444 (2007)
53. Mandelbaum R, Hirata CM, Ishak M, Seljak U, Brinkmann J. *MNRAS* 367:611 (2006a)
54. Hirata CM, Mandelbaum R, Ishak M, Seljak U *MNRAS* 381:1197 (2007)
55. Heymans C, White M, Heavens A, Vale C, van Waerbeke L *MNRAS* 371:750 (2006)
56. Ma Z, Hu W, Huterer, D *Astrophys. J* 636:21 (2006)
57. Amara A, Refregier A arXiv:0710.5171 (2007)
58. Bacon DJ, Refregier AR, Ellis RS *MNRAS* 318:625 (2000)
59. Kaiser N, Wilson G, Luppino GA arXiv:astro-ph/0003338 (2000)
60. van Waerbeke L, et al. *Astron. Astrophys* 358:30 (2000)
61. Wittman DM, et al. *Nature* 405:143 (2000)
62. Hoekstra H., Yee HKC, Gladders MD *Astrophys. J.* 577:595 (2002)
63. van Waerbeke L, Mellier Y, Hoekstra H *Astron. Astrophys* 429:75 (2005)
64. Jarvis M, Jain B, Bernstein G, Dolney D *Astrophys. J.* 644:71 (2006)
65. Hettterscheidt M, Simon P, Schirmer M, Hildebrandt H, Schrabback T, Erben T, Scheider P *Astron. Astrophys* 468:859 (2007)
66. Fu L, et al. arXiv:astro-ph/0712.0884 (2007)
67. Massey R, et al. *Astrophys. J. Supp.* 172, 239 (2007)
68. Hoekstra H et al. *Astrophys. J.* 647:116 (2006)
69. Kitching TD, Heavens AF, Taylor AN, Brown ML, Meisenheimer K, Wolf C, Gray ME, Bacon DJ *MNRAS* 771:778 (2007)

70. Massey R, et al. *Nat.* 445, 286 (2007)
71. Semboloni E, et al. *Astron. Astrophys* 452:51 (2006)
72. Benjamin J, et al. *MNRAS* 381:702 (2007)
73. Semboloni E, van Waerbeke L, Heymans C, Hamana T, Colombi S, White M, Mellier Y *MNRAS* 375, 6 (2007)
74. Ilbert O, et al. *Astron. Astrophys* 457:841 (2006)
75. Henry JP *Astrophys. J.* 609:603 (2004)
76. Rosati P, Borgani S, Norman C *Annu. Rev. Astron. Astrophys.* 50, 539 (2002)
77. Spergel DN, et al. *Astrophys. J. Supp.* 170:377 (2007)
78. Kaiser N, Squires G *Astrophys. J.* 404:441 (1993)
79. Seitz S, Schneider P *Astron. Astrophys* 305:383 (1996)
80. Seitz S, Schneider P *Astron. Astrophys* 374:740 (2001)
81. Squires G, Kaiser N *Astrophys. J* 473:65 (1996)
82. Jee MJ et al. *Astrophys. J.* 661:728 (2007)
83. Mahdavi A, Hoekstra H, Babul A, Balam DD, Capak PL *Astrophys. J.* 668:806 (2007)
84. Angus GW, Shan H, Zhao H, Famaey B *Astrophys. J.* 654:L13 (2007)
85. Milgrom, M *Astrophys. J.* 270:365 (1983)
86. Bekenstein J *Phys. Rev. D* 70:3509 (2004)
87. Bahcall NA, et al. *Astrophys. J.* 585:182 (2003)
88. Levine ES, Schulz AE, White M *Astrophys. J.* 577:569 (2002)
89. Wittman DM, Dell'Antonio IP, Hughes JP, Margoniner VE, Tyson JA, Cohen JG, Norman D *Astrophys. J.* 643:128 (2006)
90. Miyazaki S, et al. *Astrophys. J.* 580:L97 (2002)
91. Miyazaki S, Hamana T, Ellis RS, Kashikawa N, Massey, Richard J, Taylor J, Refregier A *Astrophys. J.* 669:714 (2007)
92. White M, van Waerbeke L, Mackey J *Astrophys. J.* 575:640 (2002)
93. Hennawi JF, Spergel DN *Astrophys. J.* 624:59 (2005)
94. Marian L, Bernstein GM *Phys. Rev. Lett.* 73:123525 (2006)
95. Sheldon ES, et al. arXiv:astro-ph/0709.1153 (2007)
96. Johnston DE, et al. arXiv:astro-ph/0709.1159 (2007)
97. Metzler CA, White M, Norman M, Loken C *Astrophys. J.* 520:L9 (1999)
98. Metzler CA, White M, Loken C *Astrophys. J.* 547:560 (2001)

99. Hoekstra H *Astron. Astrophys* 370:743 (2001)
100. Dahle H, Kaiser N, Irgens RJ, Lilje PB, Maddox SJ *Astrophys. J. Supp.* 139:313 (2002)
101. Hoekstra H *MNRAS* 379:317 (2007)
102. Bardeau S, Soucail G, Kneib J-P, Czoske O, Ebeling H, Hudelot P, Smail I, Smith GP *Astron. Astrophys* 470:449 (2007)
103. Mahdavi A, Hoekstra H, Babul A, Henry JP *MNRAS* in press (2008)
104. Nagai D, Vikhlinin A, Kravtsov AV *Astrophys. J.* 655:98 (2007)
105. Navarro JF, Frenk C, White SDM *Astrophys. J.* 462:563 (1996)
106. Navarro JF, Frenk C, White SDM *Astrophys. J.* 490:493 (1997)
107. Moore B, Quinn T, Governato F, Stadel J, Lake G *MNRAS* 310:1147 (1999)
108. Navarro JF, Hayashi E, Power C, Jenkins AR, Frenk CS, White SDM, Springel V, Stadel J, Quinn TR *MNRAS* 349:1039 (2004)
109. Spergel DN, Steinhardt PJ *Phys. Rev. Lett* 84:3760 (2000)
110. Meneghetti M, Yoshida N, Bartelmann M, Moscardini L, Springel V, Tormen G, White SDM *MNRAS* 325:435 (2001)
111. Flores RA, Primack JR *Astrophys. J.* 427:L1 (1994)
112. Moore B *Nature* 370:629 (1994)
113. McGaugh SS, de Blok WJG *Astrophys. J.* 499:41 (1998)
114. Treu T, Koopmans LVE *Astrophys. J.* 575:87 (2002)
115. Koopmans LVE, Treu T, Bolton AS, Burles S, Moustakas LA *Astrophys. J.* 659:599 (2006)
116. Bolton AS, Rappaport S, Burles S *Phys. Rev. D* 74:061501 (2006)
117. Comerford JM, Meneghetti M, Bartelmann M, Schirmer M *Astrophys. J.* 642:39 (2006)
118. Sand DJ, Treu T, Smith GP, Ellis RS *Astrophys. J.* 604:88 (2004)
119. Meneghetti M, Bartelmann M, Jenkins A, Frenk C *MNRAS* 381:171 (2007)
120. Dalal N, Keeton CR arXiv:astro-ph/0312072 (2003)
121. Bartelmann M, Meneghetti M *Astron. Astrophys* 418:413 (2004)
122. Mandelbaum R, Seljak U, Cool RJ, Blanton M, Hirata CM, Brinkmann J. *MNRAS* 372:758 (2006d)
123. Comerford JM, Natarajan P, *MNRAS* 379:190 (2007)
124. Broadhurst T, Takada M, Umetsu K, Kong X, Arimoto N, Chiba M, Futa-

- mase T *Astrophys. J.* 619:L143 (2005)
125. Hoekstra H., Yee HKC, Gladders MD *Astrophys. J.* 606:67 (2004)
126. Sheldon ES, et al. *Astron. J.* 127:2544 (2004)
127. Brainerd TG, Blandford RD, Smail I *Astrophys. J.* 466:623 (1996)
128. Hudson MJ, Gwyn SDJ, Dahle H, Kaiser N *Astrophys. J.* 503:531 (1998)
129. Fischer P, et al. *Astron. J.* 120:1198 (2000)
130. Mandelbaum R, Seljak U, Kauffmann G, Hirata C, Brinkmann J. *MNRAS* 368:715 (2006b)
131. Parker LC, et al. *Astrophys. J.* 669:21 (2007)
132. Dubinski J, Carlberg RG *Astrophys. J.* 378:496 (1991)
133. Mandelbaum R, Hirata C, Broderick T, Seljak U, Brinkmann J. *MNRAS* 370:1008 (2006c)
134. Mortlock DJ, Turner EL *MNRAS* 327:557 (2001)
135. Broadhurst TJ, Taylor AN, Peacock JA *Astrophys. J.* 438:49 (1995)
136. Scranton R, Menard B, Richards GT, Nichol RC *Astrophys. J.* 633:589 (2005)
137. Heavens A *MNRAS* 343:1327 (2003)
138. Taylor AN arXiv:astro-ph/0111605 (2001)
139. Hu W, Keeton CR *Phys. Rev. D* 66:063506 (2002)
140. Irwin J, Shmakova M arXiv:astro-ph/0308007 (2003)
141. Goldberg DM, Bacon DJ *Astrophys. J.* 619:741 (2005)
142. Zaldarriaga M, Seljak U *Phys. Rev. Lett* 58:023003 (1998)
143. Hu W *Astrophys. J.* 557:L79 (2001)
144. Seljak U, Hirata CM *Phys Rev D* 69:043005 (2004)
145. Zahn O, Zaldarriaga M *Astrophys. J.* 653:922 (2006)
146. Zhang P, Pen U-L *MNRAS* 367:169 (2006)
147. Metcalf RB, White SDM *MNRAS* 381:447 (2007)